Measurement Science and Technology

PAPER

Interferometric measurement of freeform surfaces using irregular subaperture stitching

To cite this article: Zhongming Zang *et al* 2020 *Meas. Sci. Technol.* **31** 055202

IOP Publishing Measurement Science and Technology
Meas. Sci. Technol. **31** (2020) 055202 (10pp) https://doi.org/10.1088/1361-6501/ab3be3

Interferometric measurement of freeform surfaces using irregular subaperture stitching

Zhongming Zang[1], Jian Bai[1], Dong Liu[1], Yuling Liu[1], Yuhao Zhou[1], Tu Shi[1], Lei Zhang[1], Liang Miao[2] and Wei Huang[2]

[1] State Key Lab. of Modern Optical Instrumentation, College of Optical Science and Engineering, Zhejiang University, Hangzhou, Zhejiang 310027, People's Republic of China
[2] State Key Lab. of Applied Optics, Changchun Institute of Optics, Fine Mechanics and Physics, Chinese Academy of Sciences, Changchun, Jilin 130033, People's Republic of China

E-mail: bai@zju.edu.cn and liudongopt@zju.edu.cn

Received 3 June 2019, revised 3 August 2019
Accepted for publication 16 August 2019
Published 31 January 2020

Abstract

Irregular subaperture stitching interferometry (ISSI) is proposed for non-null optical freeform surface testing. Compared with circular and annular subapertures, irregular subapertures have a better performance in matching the locally resolvable interferograms due to the rotational asymmetry of freeform surfaces. A modified multi-aperture simultaneous reverse optimization reconstruction algorithm is employed for the subaperture stitching, allowing not only non-complementary subapertures but also no subaperture overlaps. Numerical simulations with error analyses display the accuracy of our method. Experiments showing the effectiveness of the ISSI are presented by testing a Φ20 mm biconic surface with cross-validation.

Keywords: freeform surface, surface measurement, interferometry, subaperture stitching technology

(Some figures may appear in colour only in the online journal)

1. Introduction

Optical freeform surfaces provide a higher degree of freedom compared to rotationally symmetric elements. Since fewer optical components may be employed to meet the requirements, the use of freeform surfaces in optical designs leads to smaller, lightweight systems [1]. However, the application of the freeform surfaces is limited by the accuracy of measurement.

So far, many approaches have been developed to measure the freeform surface, such as coordinate measuring machines [2], wavefront sensors [3], fringe projection [4] and interferometry [5–11], among which interferometry is one of the most accurate methods. With special null optics, null interferometry [5–7] can achieve high-precision measurement. However, every test surface with a different nominal shape requires its own unique auxiliary optics, which results in high time and cost consumption. On the contrary, non-null interferometry, such as tilted wave interferometers [8–10] and lateral shearing interferometers [11], can provide better versatility with a retrace error correction algorithm. To test larger surfaces and extend the dynamic range with high resolution, a subaperture stitching technique is also a good solution. Surfaces exhibiting rotational symmetry, such as spheres and aspheres, can be measured with circular subaperture stitching [12–16] or annular subaperture stitching [17–19] by employing high-precision mechanical stages. However, when applied to freeform surface testing, standard circular or annular subapertures with resolvable fringes would be difficult or even impossible to obtain due to the rotational asymmetry of the test part. Moreover, the requirements for mechanical alignment are much higher, and the total number of subapertures may be very large, causing stitching complications.

In this paper, we propose an irregular subaperture stitching interferometry (ISSI) method for non-null freeform surface testing. With irregular subapertures, locally resolvable fringes

of an interferogram are matched more easily than with circular or annular ones. The total number of subapertures is therefore reduced at the same time. A multi-aperture, simultaneous reverse optimization reconstruction (SROR) algorithm [19–21] has been proposed for non-null subaperture stitching and retrace error correction in our previous work. The method is modified here to better accomplish irregular subaperture stitching. With the modified multi-aperture simultaneous reverse optimization reconstruction (MSROR) algorithm, the full aperture figure error of the test surface can be acquired at one time based on multi-configuration system modeling. In particular, overlaps and complementary requirements of the subapertures are not necessary in ISSI.

In section 2, the ISSI, involving subaperture partition principles and the MSROR algorithm, is presented. Section 3 gives the numerical simulations for the accuracy analyses and the error considerations of the ISSI. In section 4, experiments are carried out showing the practical feasibility. Conclusions are summarized in section 5.

2. Irregular subaperture stitching interferometry

The non-null interferometric system based on a Twyman–Green configuration for freeform surface test is illustrated in figure 1. A collimated laser beam ($\lambda = 632.8\,\text{nm}$) is split by a beam splitter. One beam passes through a partial null lens (PNL) [22] and is then reflected by a freeform surface under test (FS), forming a test beam after traveling through the PNL again. The other is reflected by a reference mirror, serving as the reference beam. The two beams interfere and an interferogram is captured by the detector (charge coupled device; CCD) through the imaging lens. The phase of the interferogram is modulated by a piezoelectric transducer (PZT) mounted on the reference mirror, so the wavefront data of the interferograms can be extracted with a phase-shifting algorithm. The distance between the PNL and the FS (d_{pf}) is monitored with the help of a displacement measuring interferometer (DMI).

The PNL is the key component of the ISSI system, employed to produce an aspheric reference wavefront to compensate for the majority of the longitudinal normal aberration of the FS. Unlike null interferometers, the reflected rays from the test surface may slightly deviate from the incident ones, leading to a retrace error. In addition, although the slope of the test wavefront is greatly reduced by the PNL, it is still difficult to get a resolvable interferogram over the full aperture at once due to the large degree of freedom and the asymmetry of freeform surfaces. Therefore, the subaperture stitching technique is necessary. After collecting all the subaperture wavefronts, each subaperture measurement configuration is modeled in a raytracing program according to the parameters of the actual setup. The MSROR algorithm can simultaneously achieve subaperture stitching and retrace error correction based on multi-configuration computer modeling. An elaboration for system modeling has been presented in our previous work [19]. As long as the subaperture interferograms are resolvable and the data vacancy is less than 10%, the freeform surface can be measured.

The whole measurement process is described as follows:

(a) Set up a model which is identical to the ISSI system in a raytracing program and calculate the axial range used to obtain subapertures.
(b) Change the location of the FS in the range and capture interferograms until zones with resolvable fringes cover most of the aperture. Meanwhile, update the multi-configuration model characterizing each subaperture measurement.
(c) Partition irregular subapertures according to specific principles.
(d) Accomplish the irregular subaperture stitching while correcting the retrace error by the MSROR algorithm; reconstruct the full aperture figure error of the FS.

2.1. Subaperture partition

Relying on the system model and the nominal shape of the FS, the axial distance range used to acquire subaperture interferograms can be computed. When testing, the FS is moved gradually along the optical axis in the range; slight posture adjustment can be employed at the same time, as shown in figure 2. The wavefronts at different locations match the slopes in local zones on the FS, making the slope of reflected wavefronts less than the Nyquist frequency. The resolvable fringes of different zones are recorded until most of the aperture is covered. After an interferogram is obtained at a new location (d_{pf}), a new configuration needs to be added in the model, and the only difference in all the interferometric configurations is the distance between the PNL and the FS. Note that the positions of the FS, such as axial location, tilt and decentration, may differ in the acquiring of resolvable fringes, thus these positions should be solved according to the interferograms and d_{pf} using certain algorithms [23]. Then the misalignment between the FS in the model and the actual one can be corrected.

Obviously, neither the locally resolvable areas of the interferogram nor the corresponding zones on the FS are stand shapes. Take figure 2(a) for instance, where only the upper part of the interferogram can be resolved. If circular subapertures are utilized for information extraction as plotted in figure 3(a), only a portion of the resolvable area remains in the biggest central circular subaperture. To better match the residual fringes, eight more inappropriate subapertures with different sizes have to be included. Moreover, for freeform surfaces testing, a circular subaperture in the interferogram is generally not relevant to a circular subaperture of the test part, making the stitching more complicated. As can be seen in figure 3(b), it is unfeasible for the annular subaperture which contains unresolvable areas. However, if irregular subapertures, such as semicircular, triangular and sectorial ones, are employed as exhibited in figure 3(c), the resolvable fringes are fully matched and the number of the subapertures can be reduced at the same time.

During the irregular subaperture partition of the locally resolvable interferogram for information extraction, several

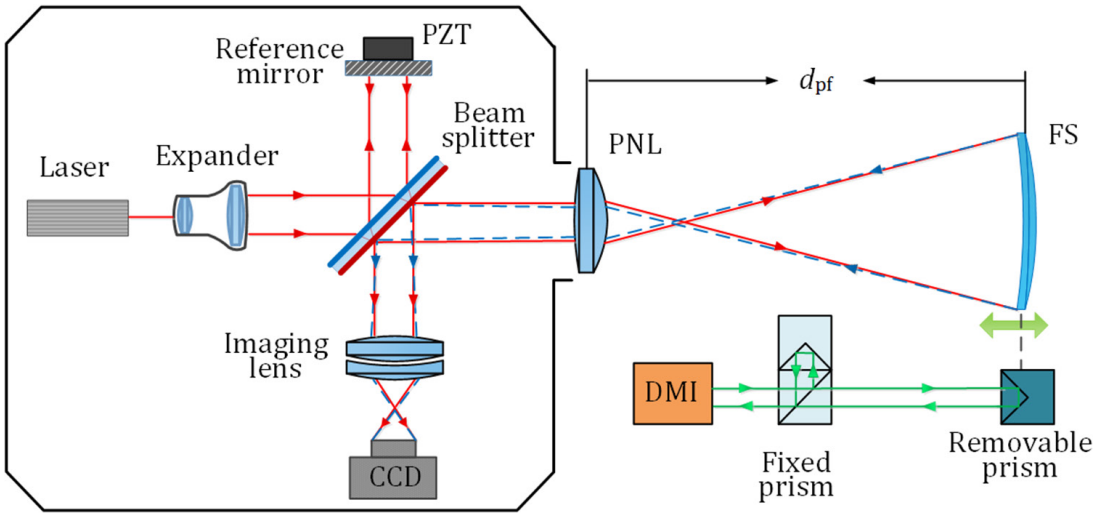

Figure 1. Sketch of the irregular subaperture stitching interferometry (ISSI) system.

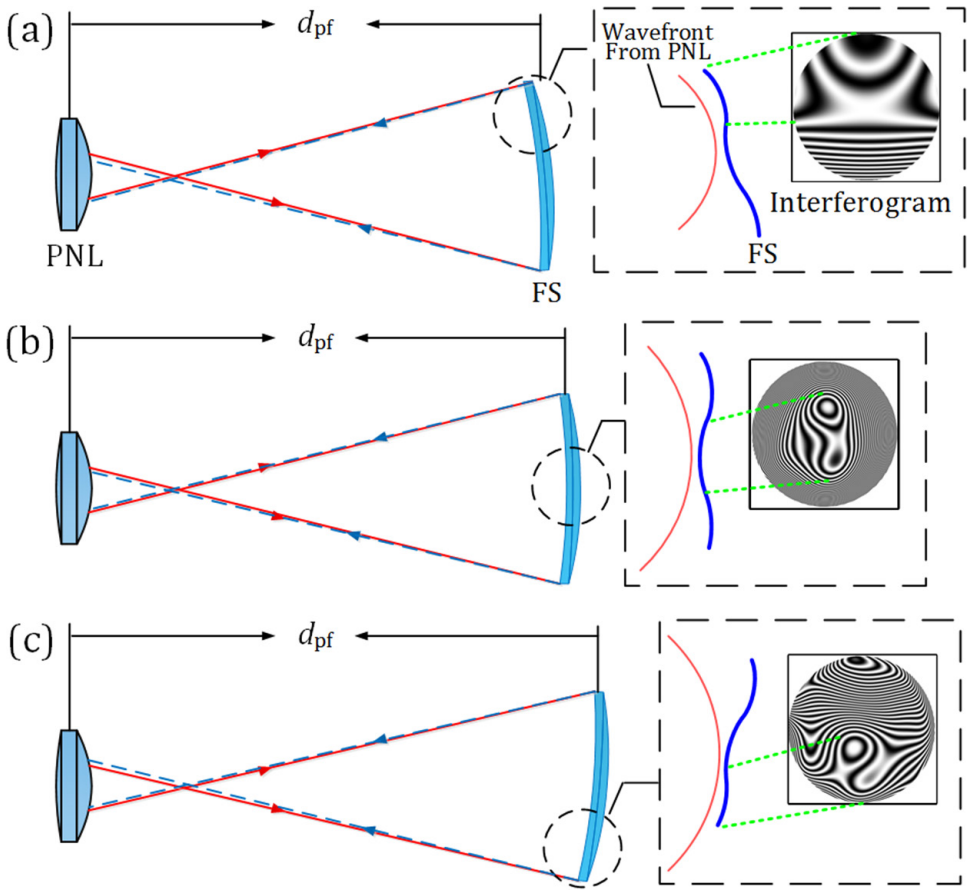

Figure 2. Locally resolvable interferograms at different location in the irregular subaperture stitching interferometry (ISSI) system. The red solid line represents the aspheric wavefront generated by the partial null lens (PNL) and the blue solid line is the freeform surface (FS).

principles should be followed. Firstly, the frequency of fringes in the subapertures should be limited within the resolution of the detector. Unlike testing rotationally symmetric optics, in which the fringe frequency usually varies along the radial direction, various directions may exist in different areas when measuring freeform surfaces. Examples of testing a biconic surface at two different locations are shown in figures 4(a) and (d). The boundary of irregular subapertures should be determined perpendicular to the maximum variation direction, making the fringe frequency in subapertures less than a threshold, which is $0.125\lambda/\text{pixel}$ in the example. Following the criteria, the partition results of figures 4(a) and (d) are shown in figures 4(b) and (e). Secondly, the obtained subapertures should be further trimmed to relatively simple shapes such as a polygons, sectors, annular sectors or ellipses, which can be described by mathematical expressions. The wavefronts in

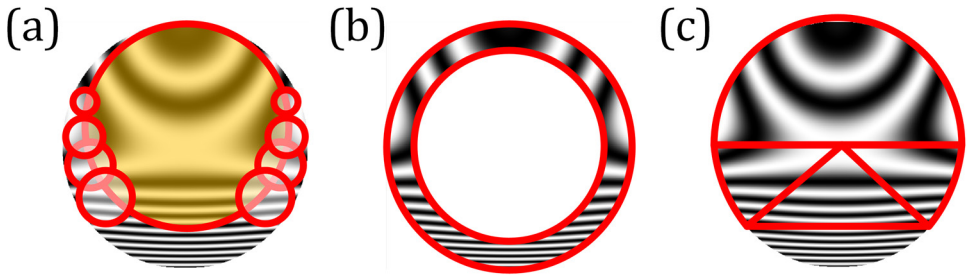

Figure 3. Subaperture partition to match locally resolvable interferogram with (a) circular subapertures, (b) annular subapertures and (c) irregular subapertures.

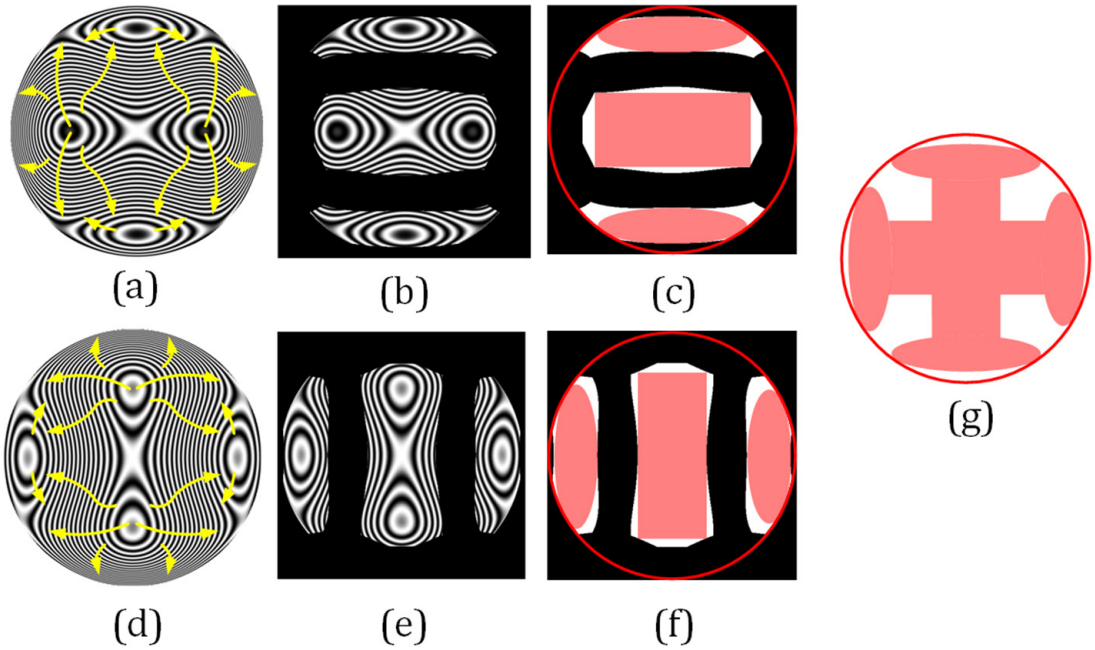

Figure 4. Irregular subaperture partition of locally resolvable interferograms. (a) and (d) are interferograms of a tested biconic surface, where the yellow arrows indicate the maximum variation directions of fringe frequency in certain areas. (b) and (d) are subapertures within the resolution; (c) and (f) are the trimmed subapertures of (b); (c) and (g) is the ultimate result of the subaperture partition.

the shapes are easier to express by orthogonal polynomials, simplifying the figure error reconstruction algorithm. For instance, figures 4(b) and (e) can be trimmed to figures 4(c) and (f) with ellipses and rectangles. Figure 4(g) displays the ultimate result of the subaperture partition.

The above processes cannot ensure that these trimmed subapertures share overlaps or cover the whole test surface; however, these conditions are not necessary in our method. Even if overlaps exist, it is also not easy to describe their boundaries due to the various shapes of the adjacent irregular subapertures. The retrace error of each subaperture needs a correction, as well. The MSROR algorithm is employed here for retrace error correction and irregular subaperture stitching without overlaps.

2.2. Full aperture figure error reconstruction: MSROR algorithm

Based on system modeling with careful calibration and reverse optimization [19, 20, 22, 24], the full aperture figure error of the test part can be optimally solved by matching the wavefronts in the model to those in the experiment. If the system is modeled consistently with the actual one, then the wavefront at the image plane in the model will also be the same as the experimentally detected wavefront when the figure error of the test part in the model is the same as the actual one to be tested. This idea still works for the wavefronts of irregular subapertures. Therefore, the multi-configuration model is established according to all the subaperture acquirement configurations. Setting the wavefronts of all subapertures detected from the actual system as targets and optimizing the full aperture figure error in the model, the figure error can be solved until each subaperture wavefront in the corresponding configuration optimally matches the targets. The figure error of the FS in every configuration is changed synchronously, that is, the optimization is carried out on all the subapertures simultaneously in the model rather than each subaperture separately.

In the MSROR algorithm, to map the full aperture figure error and the wavefronts of the irregular subapertures uniquely, polynomials which are orthogonal in the concerned zones are used as

$$\begin{cases} E_{\text{full}} \approx \sum_{i=1}^{\text{M}} B_i Z_i, \quad E^*_{\text{full}} \approx \sum_{i=1}^{\text{M}} B^*_i Z_i, \\ W_{\text{sub}|k} \approx \sum_{j=1}^{\text{N}} C_{j|k} V_{j|k}, \quad W^*_{\text{sub}|k} \approx \sum_{j=1}^{\text{N}} C^*_{j|k} V_{j|k}, \end{cases} \tag{1}$$

where E_{full} represents for the full aperture figure error of the FS and E^*_{full} is the corresponding one in the model. $W_{\text{sub}|k}$ is the detected wavefront of the kth subaperture, which can be extracted by the resolvable interferogram with a phase-shifting algorithm, and $W^*_{\text{sub}|k}$ is the corresponding wavefront in the model. Zernike standard polynomials $Z_i\,(i = 1, 2, \cdots, M)$ are used to describe the figure error, $V_{j|k}\,(j = 1, 2, \cdots, N)$ are orthogonal polynomials for the expression of the kth subaperture wavefront, M and N are the total terms of the employed polynomials. B_i and $C_{j|k}$ are the corresponding coefficients of Z_i and $V_{j|k}$ for the actual system, while B^*_i and $C^*_{j|k}$ are those for the model. The optical freeform surfaces are continuous and smooth, making it ideal to express their figure error with Zernike polynomials. The high-frequency parts of the surface deformation, which are generally referred to as 'roughness', is ignored during the polynomial fitting process and will not be discussed in this paper. Furthermore, the random error of interferograms can be suppressed by using polynomials to fit the subaperture wavefront.

Zernike annular polynomials have been employed to express the subaperture wavefront for non-null annular subaperture stitching in the SROR method [19]. However, they cannot be applied to other aperture shapes due to the non-orthogonality of the Zernike annular polynomials in non-annular zones. To describe the wavefronts of irregular subapertures, the orthogonal polynomials in the irregular zones should be found out. Although the Zernike standard polynomials lose their orthogonality in non-circular zones, they can still serve as a complete basis for the calculation of the orthogonal polynomials $V_{j|k}\,(j = 1, 2, \cdots, N)$ of arbitrary irregular zones as

$$V_{j|k} = \sum_{o=1}^{N} T_{jo|k} Z_o, \tag{2}$$

where $T_{jo|k}\,(o = 1, 2, \cdots, N)$ represents the element of the conversion matrix and Z_o is the oth Zernike standard polynomial. The conversion matrix is related to the boundary and the position of the concerned subaperture. Since the shapes of the subapertures can be described by mathematical expressions, the conversion matrices of all the irregular subapertures are easy to get; the method has been described in detail in [25].

Setting B^*_i as variables and $C_{j|k}$ as targets, we perform a raytracing of the system model after each round iterative optimization of B^*_i according to an objective function, until $C^*_{j|k}$ of all the subapertures optimally matches $C_{j|k}$. Using the experimental subaperture wavefront, $C_{j|k}$ can be calculated by the least squares fitting techniques. In each configuration of the model, it is easy to obtain the wavefront on the detector by raytracing, thus $C^*_{j|k}$ can be solved using the subaperture wavefront in the model relying on the same method as $C_{j|k}$ and then updated after each round iteration. It should be noted that one configuration may have multiple subapertures, as shown in figures 4(b) and (e). The objective function is set as

$$\begin{aligned} &O\left(\left[B^*_{1|\text{o}}, B^*_{2|\text{o}}, \cdots, B^*_{i|\text{o}}, \cdots, B^*_{M|\text{o}}\right]\right) \\ &= \min\left[\sum_{k=1}^{\text{K}} \left(W^*_{\text{sub}|k} - W_{\text{sub}|k}\right)^2\right] \\ &= \min\left\{\sum_{k=1}^{\text{K}} \left[\sum_{j=5}^{\text{N}} \left(C^*_{j|k} - C_{j|k}\right)^2\right]\right\}, \end{aligned} \tag{3}$$

where $B^*_{i|\text{o}}$ is the optimal solution of B^*_i and K is the total number of the subapertures. Since the first four Zernike polynomials are related to the misalignment error, they have no weight in the objective function. A damped least squares method is used to optimize the figure error coefficients B^*_i in the iteration. After the optimization is completed, the figure error is solved as

$$E_{\text{full}} \approx E^*_{\text{full}} \approx \sum_{i=1}^{\text{M}} B^*_{i|\text{o}} U_i. \tag{4}$$

In the MSROR process, the retrace error is corrected through reverse optimization with iterative raytracing based on system modeling. The above process can be summarized as

$$\begin{cases} E_{\text{full}} = \mathbf{F}\left\{W_{\text{sub}|1}, W_{\text{sub}|2}, \cdots, W_{\text{sub}|\text{K}}\right\}, \quad \text{or} \\ \begin{bmatrix} B^*_1 \\ B^*_2 \\ \cdots \\ B^*_{\text{M}} \end{bmatrix} = \mathbf{F} \begin{Bmatrix} \left[C_{1|1}, C_{2|1}, \cdots, C_{\text{N}|1}\right] \\ \left[C_{1|2}, C_{2|2}, \cdots, C_{\text{N}|2}\right] \\ \cdots \\ \left[C_{1|K}, C_{2|K}, \cdots, C_{\text{N}|K}\right] \end{Bmatrix}, \end{cases} \tag{5}$$

where $\mathbf{F}$ represents the function relationship. From equation (5), it is seen that the MSROR algorithm is very similar to the process in solving equations. The solution would remain correct as long as the regularity of equation (5) is not affected by a lack of data from the incomplete covering of the full aperture.

3. Numerical simulations

3.1. Full aperture figure error reconstruction

The ISSI method is carried out in a simulated freeform surface test for a biconic surface with a clear aperture of 30 mm. The nominal shape of the adopted test part is

$$z = \frac{\frac{1}{R_x}x^2 + \frac{1}{R_y}y^2}{1 + \sqrt{1 - (1 + k_x)\frac{x^2}{R_x^2} - (1 + k_y)\frac{y^2}{R_y^2}}}, \tag{6}$$

where z is the sag of the surface, $R_x = 242$ mm and $R_y = 238$ mm are the vertex radius in the x and y direction, $k_x = -1.2$ and $k_y = -0.8$ are the conic coefficients in the x and y direction. The peak-to-valley (PV) value of the surface deformation is 1.296λ ($\lambda = 632.8$ nm). A positive singlet lens is employed as the PNL, and table 1 details the parameters of the PNL. The non-null interferometer is modeled in a raytracing program according to these parameters, serving as the experimental system.

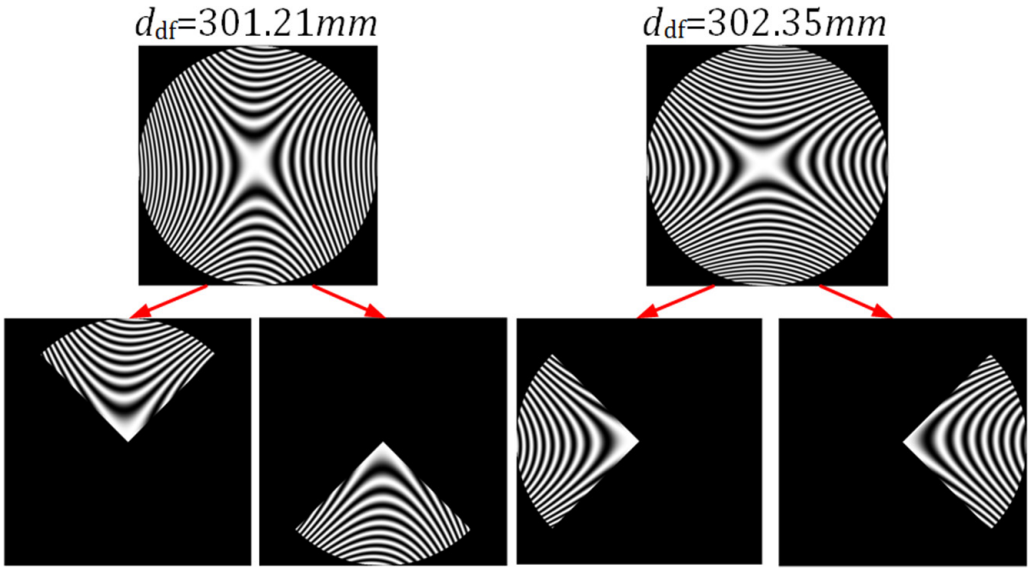

Figure 5. Interferograms of full aperture and subapertures in the simulations.

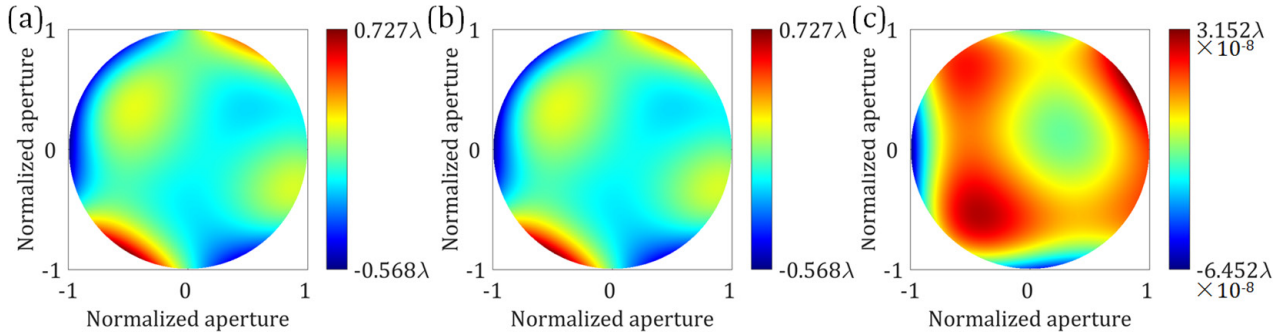

Figure 6. Figure error and residual error in the simulations. (a) Figure error reconstructed with the irregular subaperture stitching interferometry (ISSI) method. (b) Actual figure error. (c) Residual error of (a).

Two positions are selected to capture interferograms, and each interferogram corresponds to two 90-degree sectorial subapertures according to the partition principles in section 2.1, as shown in figure 5. The wavefront data ($W_{\text{sub}|k}$) of the subapertures can be easily extracted from interferograms. Fifteen orthogonal polynomials in each subaperture are calculated based on the first 15 standard Zernike polynomials, then the new polynomials are employed to fit the $W_{\text{sub}|k}$ and the coefficients ($C_{j|k}$) are obtained.

Subsequently, another similar system model which has two configurations with d_{pf} of 301.21 mm and 302.35 mm is set up to solve the figure error. The deformation of the test surface is expressed first by 15 Zernike standard polynomials, whose coefficients (B_i^*) are set as variables with all the initial values of zero, and the subaperture wavefront coefficients ($C_{j|k}$) serve as the optimization targets. Then, the MSROR algorithm is implemented for the figure error construction. After three rounds (about 6 min) of optimization, the objective function is less than 10^{-7}, and then the B_i^* is acquired. Figure 6(a) presents the figure error of the full aperture reconstructed through polynomial fitting, which is the same as the actual figure error shown in figure 6(b). Figure 6(c) illustrates the residual error in a magnitude of 10^{-8} λ, confirming the high accuracy of the ISSI method.

Table 1. Parameters of the partial null lens (PNL).

Surface	Radius (mm)	Thickness (mm)	Glass	Conic (unit)
1	89.148	10.65	K9	0
2	−50.678			0

3.2. Error analysis

The above simulation is carried out in an ideal circumstance, but the reconstruction accuracy will decrease with the increase of various errors in actual tests. The errors can be considered as coming from two parts, one being the non-null interferometer, and the other the subaperture stitching. The following will give an elaboration of these two sources of error, and their influence on reconstruction results will be analyzed based on the biconic surface simulation in section 3.1.

In non-null testing, the retrace error, interferometer system error, and fringe error always exist. The retrace error is corrected by the MSROR algorithm based on system modeling, therefore the modeling error, which refers to inaccurate modeling of the PNL and the freeform surface, directly influences the accuracy of the reconstructed figure error. With the help of commercial measurement instruments [26], the radius of

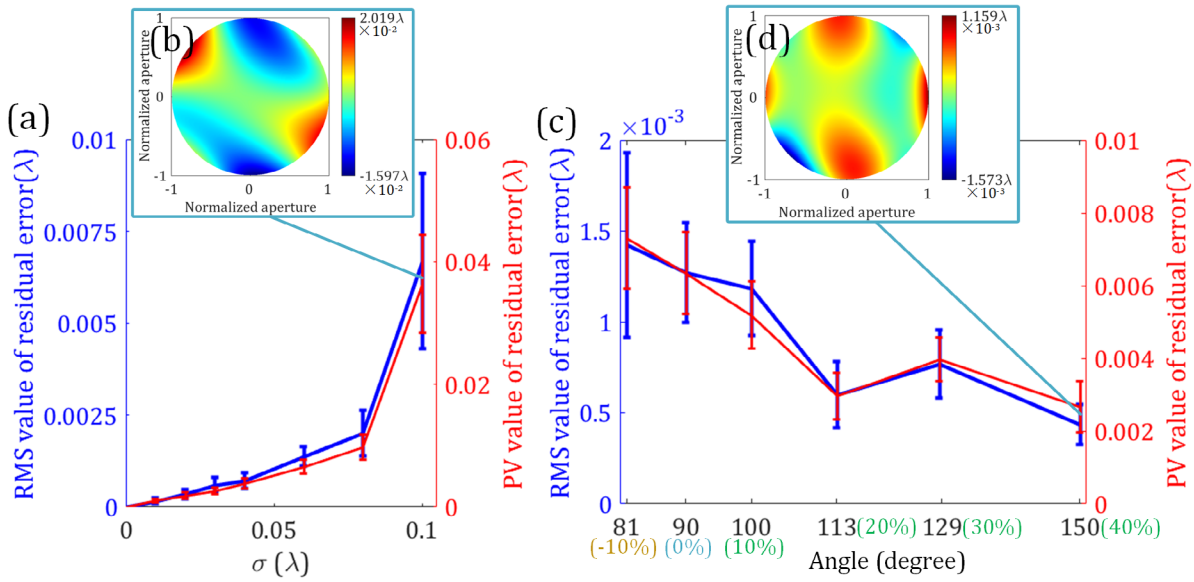

Figure 7. The effect of (a) random error and (c) subaperture overlapping region on the reconstruction accuracy. The point on the line is the average value of five simulation results, and the error bar is the standard deviation. The overlap ratio of adjacent subapertures and the ratio of data vacancy are marked by green and gold in (c). (b) is the residual error map for a representative simulation in (a) when σ is 0.1, and (d) is that in (c) when the angle of each sectorial subaperture is 150 degree.

curvature, refractive index, and thickness of the PNL can be better than $\pm 0.005\%$, $\pm 10^{-5}$, and ± 5 μm, respectively. Moreover, since the PNL is a singlet lens, the figure error of each surface is better than 0.05λ (PV value). These uncertainties result in a tiny transmission wavefront error, so the modeling error caused by the PNL is almost negligible. The modeling error of the freeform surface is due to position and location inconsistency with the experimental system, and correction of this error is discussed in [23]. The interferometer system error, which comes from the transmission and reflection wavefront error of each component, can be calibrated with a standard reflector in place of the test arm and removed. The major sources of the fringe error are interferogram random error and phase-shifting error. The random error, induced by airflow, temperature, humidity and the detector, obeys normal distribution:

$$f(x) = \frac{1}{\sigma\sqrt{2\pi}} \exp\left[\frac{-(x-\mu)^2}{2\sigma^2}\right], \tag{7}$$

where μ and σ are the average value and the standard deviation of the error x, respectively, and $f(x)$ is the probability density function. In simulations, the random error with $\mu = 0$ is added to the interferograms used in the phase-shifting algorithm. Moreover, a Gaussian filter is employed to suppress the random error. Figure 7(a) illustrates the relationship between the reconstruction residual error and σ; it is obvious that the root-mean-square (RMS) value and the PV value of the residual error increase with the rise of the random error. In a thermostatic super-clean lab, the σ can be easily controlled below 0.05λ, and the influence of the random error is further reduced by low-pass filters, phase-shifting algorithms and polynomials fitting, thus the reconstruction residual error due to the random error is smaller than 0.01λ (PV value). The positioning accuracy of the PZT is about 5 nm; as a result, the reconstruction error generated by the phase-shifting error is about 0.001λ. To sum up, the total non-null testing error effect is in a magnitude of $10^{-2}\lambda$.

As for the subaperture stitching, the MSROR algorithm allows no subaperture overlaps and small data vacancy, which is different from the conventional stitching method. When the random error is ignored in simulations, the reconstruction residual error is in a magnitude of 10^{-8} λ regardless of the overlap region, and 10% data vacancy leads to an error with a magnitude of 10^{-7} λ. Then, a random error with $\mu = 0$ and $\sigma = 0.06$ is added in simulations, the results of which are plotted in figure 7(c); the angle of each sectorial subaperture is changed to achieve overlap or data vacancy. When the angle is larger than 90 degrees, different adjacent subaperture overlap ratios can be accomplished. The ratio reflects how much of the subaperture area is occupied by the overlapped region, which is marked by green in figure 7(c). Since a larger subaperture size results in better random error immunity, the reconstruction accuracy improves as the overlap ratio increases. By reducing the angle, it can be calculated that the PV value of reconstruction residual error is better than 0.01λ when the data vacancy is 10%. Therefore, the overlap area is not necessary in the MSROR algorithm and small data vacancy is permissible, while the stitching data with overlap region, which means larger subaperture size, has a better performance in the case of the large random error. Note, that when the data vacancy is larger than 10%, the residual error increases sharply and it is hard to guarantee a successful figure error recovery. The subaperture wavefront is expressed by orthogonal polynomials which depend on the irregular zone location and area, hence the reconstruction accuracy is very sensitive to the relative position and the size of the subapertures. A 5% position or aperture error between the actual subapertures and the model ones causes an error of 0.1λ (PV value). In addition, similar to the conventional stitching algorithm, an

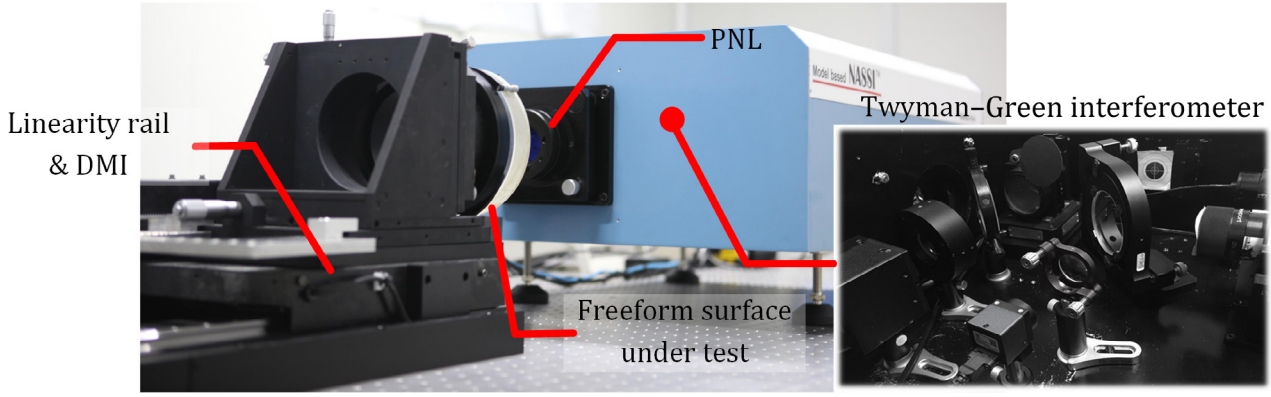

Figure 8. Experiment layout.

Table 2. Specification of the subapertures.

Subaperture	S_1	S_2	S_3	S_4
d_{pf} (mm)	301.396	301.396	302.252	302.252
Sector zone (rad)	$[\pi/4, 3\pi/4]$	$[-3\pi/4, -\pi/4]$	$[3\pi/4, 5\pi/4]$	$[-\pi/4, \pi/4]$

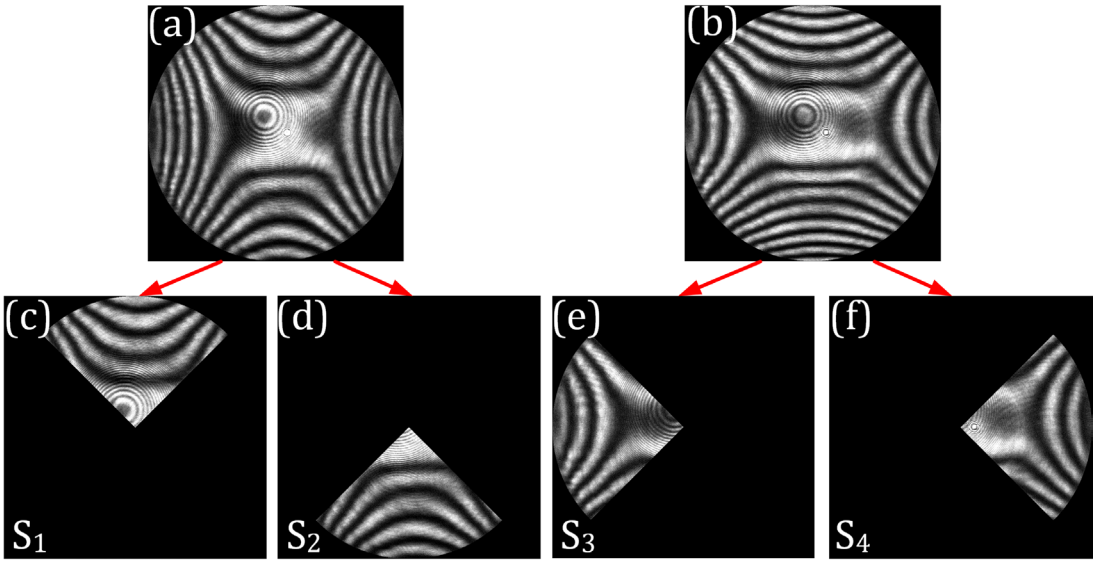

Figure 9. Interferograms. (a) and (b) are the interferograms of the full aperture with d_{pf} of 301.396 mm and 302.252 mm respectively; (c) and (d) are subapertures S_1 and S_2; (e) and (f) are subapertures S_3 and S_4.

excessive number of subapertures increases the computational complexity. When the number of subapertures is less than 20, there is no significant influence on the accuracy. In general, the error introduced by stitching is more complex than that of non-null testing system.

According to these analyses, reconstruction accuracy is between a magnitude of 10^{-1} λ and 10^{-2} λ, depending on the quality of stitching data. Data vacancy smaller than 10% and subapertures without overlaps are permissible. However, the errors may even couple with one another, making correction difficult and decreasing the reconstruction accuracy.

4. Experimental result

A biconic surface with an aperture of 20 mm was processed by a five-axis diamond turning lathe (Nanotech 350FG) to verify the practical feasibility of our method. The experiment layout is shown in figure 8; the nominal shape of the adopted test part and the PNL were consistent to those in section 3. The precision of the DMI is $\pm 0.5 \times 10^{-3}$ mm, with a measurement range of 40 m. Four sectorial subapertures at two different positions were partitioned according to the previous principles. Since there is a machining error in the radius of

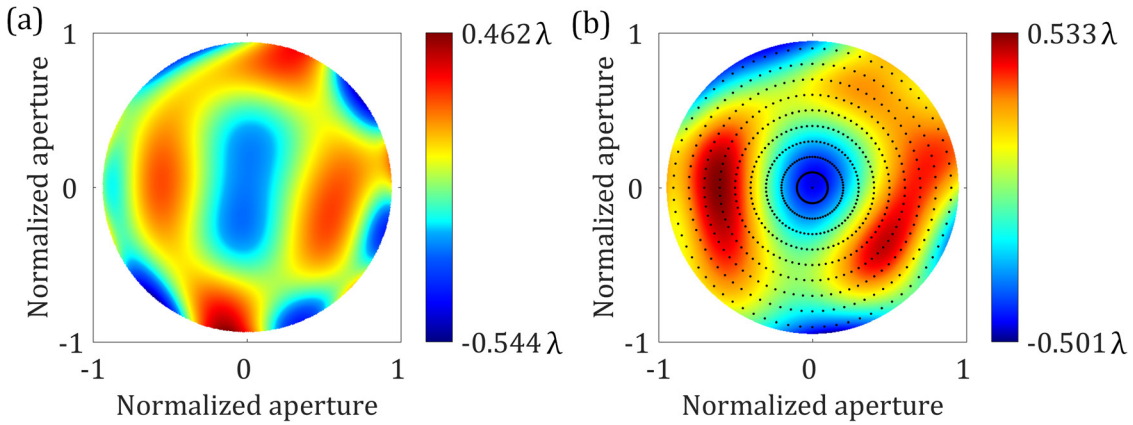

Figure 10. Testing results. (a) Reconstructed figure error with the ISSI method. (b) Figure error measured by coordinate measuring machine. The black dots in (b) are sampling points of the coordinate measuring machine (CMM) and other data is calculated by interpolation.

curvature, the positions have a tiny difference compared with the simulations. Table 2 lists the parameters of the subapertures detected at different d_{pf}; the corresponding interferograms are shown in figure 9.

According to the practical setup, two configurations with d_{pf} of 301.396 mm and 302.252 mm were modeled in a ray-tracing program [19, 23]. In the model, the figure error of the test surface was expressed first with 37 Zernike standard polynomials and the coefficients were set as variables to be optimized. To express the wavefronts in the subapertures, 37 polynomial terms that were orthogonal in the sectorial zones were calculated based on Zernike standard polynomials [25]. In the MSROR algorithm, all these coefficients were set as targets in the model simultaneously, and the figure error coefficients of the test part were iteratively optimized to make the wavefront coefficients of each subaperture in the model close to the targets. When the coefficients of each subaperture in the model matched well with those in the experiment, the variables were solved. Figure 10(a) illustrates the reconstructed figure error by polynomials fitting; the PV value and the RMS value are 1.006λ ($\lambda = 632.8$ nm) and 0.153λ, respectively. In order to verify the results of our method, the biconic surface was measured with a coordinate measuring machine (CMM) (PRISMO 9/12/7 ultra, Carl Zeiss IMT GmbH). CMMs can achieve an absolute measurement of height, while the surface deformation is obtained by subtracting the nominal shape from the results. The method is different from interferometry, which uses interference fringes for relative measurement, so we use it as a contrastive experiment. A map of the figure error measured by the CMM is plotted in figure 10(b), where the PV value and the RMS value are 1.034λ and 0.234λ, respectively. The sampling points in measurement are marked by black dots in figure 10(b) while other data are calculated by interpolation. The topography of figure 10(a) has a superior agreement with figure 10(b), confirming the practical feasibility of the ISSI method. The deviation of PV values is less than 0.03λ, while the RMS value departure is less than 0.08λ. Since the interferometer has a better horizontal resolution, especially in the edge regions, some parts and the RMS value are a little different from the results of the CMM.

5. Conclusion

We proposed an ISSI with the MSROR algorithm which can solve the full aperture figure error simultaneously and better matches the locally resolvable interferograms for freeform surface measurement. The irregular subapertures are partitioned according to specific principles and the subaperture wavefront is uniquely expressed using polynomials which are orthogonal in the concerned zones. A reverse iterative ray-tracing process is employed to extract the figure error in form of Zernike standard polynomials from the subaperture wavefront coefficients, thus no extra algorithms for retrace error correction and subaperture stitching are needed. The ISSI allows no subaperture overlaps and even small data vacancy in the non-complementary subapertures, which reduces the position adjustment of the test part and ensures relatively simple system configuration without customized null optics. Time and cost are therefore saved in the method. Both numerical simulations and experimental results show that the measurement accuracy is better than 0.05λ (PV value). However, it should be emphasized that the system model demands careful calibration and its accuracy has a great influence on the final measurement result. In addition, the measurement range of our method depends on the PNL. Thus, a series of PNLs will be designed and processed to measure freeform surfaces with larger degree of freedom in future work, and the measurement range will also be analyzed in detail.

Funding

The work was supported by National Key Research and Development Program of China (Grant No. 2016YFC1400900); National Natural Science Foundation of China (NSFC) (Grant No. 41775023); Excellent Young Scientist Program of Zhejiang Provincial Natural Science Foundation of China (Grant No. LR19D050001); Public Welfare Project of Zhejiang Province (Grant No. 2016C33004); Fundamental Research Funds for the Central Universities (Grant No. 2017QNA5001); State Key Laboratory of Modern Optical Instrumentation Innovation Program (Grant No. MOI2018ZD01).

ORCID iDs

Jian Bai https://orcid.org/0000-0002-5128-2146
Dong Liu https://orcid.org/0000-0002-2463-832X

References

[1] Cheng D, Wang Y, Hua H and Talha M M 2009 Design of an optical see-through head-mounted display with a low *f*-number and large field of view using a freeform prism *Appl. Opt.* **48** 2655–68

[2] Fang F Z, Zhang X D, Weckenmann A, Zhang G X and Evans C 2013 Manufacturing and measurement of freeform optics *CIRP Ann.* **62** 823–46

[3] Guo W, Zhao L and Chen I M 2014 Reference-free beam-sampling system for freeform surface measurements *Appl. Opt.* **53** H20–6

[4] Xiao Y-L, Xue J and Su X 2013 Robust self-calibration three-dimensional shape measurement in fringe-projection photogrammetry *Opt. Lett.* **38** 694–6

[5] Qiu G and Cui X 2013 Fermat principle based reflector design for fast and contactless freeform optical component inspections *Opt. Lett.* **38** 3510–3

[6] Fuerschbach K, Thompson K P and Rolland J P 2014 Interferometric measurement of a concave, φ-polynomial, Zernike mirror *Opt. Lett.* **39** 18–21

[7] Xue S, Chen S, Tie G and Tian Y 2019 Adaptive null interferometric test using spatial light modulator for free-form surfaces *Opt. Express* **27** 8414–28

[8] Garbusi E, Pruss C and Osten W 2008 Interferometer for precise and flexible asphere testing *Opt. Lett.* **33** 2973–5

[9] Li J, Shen H, Zhu R, Gao J, Sun Y, Wang J and Li B 2018 Interferometry with flexible point source array for measuring complex freeform surface and its design algorithm *Opt. Commun.* **417** 67–75

[10] Hao Q, Wang S, Hu Y, Cheng H, Chen M and Li T 2016 Virtual interferometer calibration method of a non-null interferometer for freeform surface measurements *Appl. Opt.* **55** 9992–10001

[11] Ghim Y-S, Rhee H-G, Davies A, Yang H-S and Lee Y-W 2014 3D surface mapping of freeform optics using wavelength scanning lateral shearing interferometry *Opt. Express* **22** 5098–105

[12] Küchel M F 2009 Interferometric measurement of rotationally symmetric aspheric surfaces *Proc. SPIE* **10316** 103160Q

[13] Murphy P, DeVries G, Fleig J, Forbes G, Kulawiec A and Miladinovic D 2009 Measurement of high-departure aspheric surfaces using subaperture stitching with variable null optics *Proc. SPIE* **7426** 74260P

[14] Zhang P, Zhao H, Zhou X and Li J 2010 Sub-aperture stitching interferometry using stereovision positioning technique *Opt. Express* **18** 15216–22

[15] Liang C-W, Chang H-S, Lin P-C, Lee C-C and Chen Y-C 2013 Vibration modulated subaperture stitching interferometry *Opt. Express* **21** 18255–60

[16] Yan L, Wang X, Zheng L, Zeng X, Hu H and Zhang X 2013 Experimental study on subaperture testing with iterative triangulation algorithm *Opt. Express* **21** 22628–44

[17] Chen S, Li S, Dai Y, Ding L and Zeng S 2008 Experimental study on subaperture testing with iterative stitching algorithm *Opt. Express* **16** 4760–5

[18] Zhang L, Tian C, Liu D, Shi T, Yang Y, Wu H and Shen Y 2014 Non-null annular subaperture stitching interferometry for steep aspheric measurement *Appl. Opt.* **53** 5755–62

[19] Zhang L, Liu D, Shi T, Yang Y, Chong S, Ge B, Shen Y and Bai J 2015 Aspheric subaperture stitching based on system modeling *Opt. Express* **23** 19176–88

[20] Liu D, Zhou Y, Bai J, Shi T, Shen Y, Yang Y and Zhang L 2016 Aspheric and free-form surfaces test with non-null sub-aperture stitching *Proc. SPIE* **10021** 100210N

[21] Zhang L, Li D, Liu Y, Liu J, Li J and Yu B 2017 Validation of simultaneous reverse optimization reconstruction algorithm in a practical circular subaperture stitching interferometer *Opt. Commun.* **403** 41–9

[22] Liu D, Shi T, Zhang L, Yang Y, Chong S and Shen Y 2014 Reverse optimization reconstruction of aspheric figure error in a non-null interferometer *Appl. Opt.* **53** 5538–46

[23] Zang Z *et al* 2019 Misalignment correction for free-form surface in non-null interferometric testing *Opt. Commun.* **437** 204–13

[24] Gappinger R O and Greivenkamp J E 2004 Iterative reverse optimization procedure for calibration of aspheric wavefront measurements on a nonnull interferometer *Appl. Opt.* **43** 5152–61

[25] Dai G-M and Mahajan V N 2007 Nonrecursive determination of orthonormal polynomials with matrix formulation *Opt. Lett.* **32** 74–6

[26] TRIOPTICS 2019 SpectroMaster retrieved (www.trioptics.com/products/goniometer-spectrometer/spectromasterr-hr-universal/)